Chapter 20
Swarming of Self-propelled Particles on the Surface of a Thin Liquid Film

Andrey Pototsky, Uwe Thiele and Holger Stark

Abstract We consider a colony of self-propelled particles (swimmers) in a thin liquid film resting on a solid plate with deformable liquid-gas interface. Individual particles swim along the surface of the film predominantly in circles and interact via a short range alignment and longer-range anti-alignment. The local surface tension of the liquid-gas interface is altered by the local density of swimmers due to the soluto-Marangoni effect. Without the addition of swimmers, the flat film surface is linearly stable. We show that a finite wave length instability of the homogeneous and isotropic state can be induced by the carrier film for certain values of the rotational diffusivity and a nonzero rotation frequency of the circular motion of swimmers. In the nonlinear regime we find square arrays of vortices, stripe-like density states and holes developing in the film.

20.1 Introduction

Emerging spatio-temporal density and velocity patterns in suspensions of motile living cells became the focus of many experimental and theoretical studies over the last decade. With the typical body size of several μm, the colonies of swimmers exhibit a wide range of meso-scale and large-scale coherent structures such as circular vortices, swirls and meso-scale turbulence with the correlation length of the collective motion ranging between $\sim$10 and $\sim$100 μm [6, 10, 12, 19–23, 27].

A. Pototsky (✉)
Department of Mathematics, Faculty of Science Engineering and Technology, Swinburne University of Technology, Hawthorn, VIC 3122, Australia
e-mail: apototskyy@swin.edu.au

U. Thiele
Institut für Theoretische Physik, Westfälische Wilhelms-Universität Münster, 48149 Münster, Germany

H. Stark
Institut für Theoretische Physik, Technische Universität Berlin, Hardenbergstraße 36, 10623 Berlin, Germany

E. Schöll et al. (eds.), *Control of Self-Organizing Nonlinear Systems*, Understanding Complex Systems, DOI 10.1007/978-3-319-28028-8_20

It was recognized that the onset of the observed large-scale patterns is associated with a finite wave length instability of the homogeneous and isotropic distribution of swimmers [2]. Recently, a minimal phenomenological model of the spatio-temporal pattern formation of living matter was developed on the basis of a Swift-Hohenberg type scalar field theory [7]. The physical mechanism, underlying the instability was traced down to the short-range aligning and longer-range anti-aligning interaction between the orientation of swimmers [9]. On the microscopic level, the short-range alignment can be explained by the collisions between swimmers with elongated bodies, or by flagellar bundling [27]. The longer-range anti-alignment is linked to hydrodynamic interactions [9] that are known to destabilize the polar order at high densities.

In experiments with bacterial suspensions confined between solid boundaries, the role of the solvent fluid is seen as a passive carrier that gives rise to hydrodynamic interactions between individual swimmers. However, in the case of freely suspended soaplike liquid films loaded with bacteria, the deformations of the liquid-gas interface and the resulting motion of the carrier fluid can no longer be neglected. Thus, in the early experiments with *E. coli* bacteria [29], a droplet of bacterial suspension was stretched between 10 μm thin fibers to form a soaplike film. In order to delay the film rupture, a stabilizing chemical surfactant had to be added. In later studies with 1 μm soaplike films, metabolic products, secreted by the *B. subtilis* bacteria, played the role of the stabilizing surfactant [20–22]. Without the addition of a stabilizing surfactant, the life time of the film is determined by the film thickness and the surface tension. In most recent experiments with *E. coli* bacteria, the rupture of a 20 μm film was detected after several minutes [12].

Motivated by these recent experiments, we address here the question of how a suspension of swimmers, confined to move in a thin liquid film on a solid substrate, is affected by the presence of a deformable liquid-gas interface. To this end, we consider a non-evaporating 10–100 μm thin liquid film with a deformable liquid-gas interface, resting on a solid plate. Lubrication theory [14] predicts that without the addition of swimmers, the flat film is linearly stable, with respect to small amplitude variations of its thickness. The film is loaded with surface swimmers that interact with each other via a short-range alignment and longer-range anti-alignment, as described in [9]. In case of the resting fluid, a homogeneous and isotropic distribution of swimmers is linearly unstable with respect to a finite wave length instability.

We extend the model of self-propelled particles, used in Ref. [9], by additionally taking into account a deterministic rotation of the bodies of individual swimmers that gives rise to their circular motion. Thus, it is known that bacteria with helical flagellas swim in circles, predominantly clockwise near a solid-liquid interface and anticlockwise near a liquid-gas interface [5, 8]. We neglect steric repulsion between the swimmers and introduce their translational surface diffusion.

As suggested by earlier studies, the coupling between the swimmers and the liquid film occurs through the soluto-Marangoni effect [1, 18]. Indeed, some living cells, such as *B. subtilis* bacteria, excrete metabolic products [21] that act as a surfactant and change the local surface tension of the liquid film. Consequently, the local concentration of the surfactant particles is proportional to the local concentra-

tion of swimmers. It should be emphasized that the surface tension decreases with the surfactant concentration, implying that soluto-Marangoni effect stabilizes a flat film [14].

Our resulting model consists of the thin film equation for the local film thickness, coupled to the Smoluchowski equation for the swimmer density distribution function. In the coupled system, the emergence of a density patterns always occurs in conjunction with film surface deformations. We find that a seemingly passive liquid film has a profound effect on the linear stability of a homogeneous isotropic distribution of swimmers on the surface of a flat film. In particular, there exists a window of parameters, for which the isotropic state is linearly stable in the absence of the liquid film and is linearly unstable when the liquid film is included.

By numerically solving the evolution equations for film height and swimmer density, we find square arrays of vortices for parameter combinations close to the instability threshold. Deep in the unstable region, we find stripes in the density distribution for small values of the self-propulsion velocity. These long-lasting states are accompanied by stripe-like small amplitude deformations of the film surface. Typically the stripes on the film surface are in antiphase with the density stripes. For large self-propulsion velocities, we demonstrate the development of a depression region on the film surface that has a lateral size comparable to the system size. The depth of the depression gradually increases with time, thus, increasing the probability of film rupture. In our numerical simulations we have observed film rupture at finite times.

20.2 Model Equations

Consider a colony of active Brownian particles that swim along the liquid-gas interface of a thin liquid film. The swimming direction of the ith particle is given by the unit vector $\boldsymbol{p}_i$, which is tangential to the liquid-gas interface at all times. We only take into account long wavelength deformations of the liquid-gas interface at height $h(x, y)$, whereby the gradient ∇h is small at all times. In this case, the orientation vector $\boldsymbol{p}_i$ is approximately two-dimensional $\boldsymbol{p}_i = (\cos(\phi), \sin(\phi))$, where ϕ denotes the polar angle.

The interaction between the swimmers is characterized by pair-wise alignment at short distances and anti-alignment at large distances. The interaction strength is given by a certain coupling function $\mu(|\boldsymbol{r}_i - \boldsymbol{r}_j|)$ of the separation distance $|\boldsymbol{r}_i - \boldsymbol{r}_j|$ between the ith and the jth swimmer. Positive (negative) values of $\mu(r)$ correspond to pair-wise alignment (anti-alignment) [9].

The stochastic equations of motion for the ith swimmer can be written as

$$\begin{aligned} \dot{\boldsymbol{r}}_i &= v_0 \boldsymbol{p}_i + \boldsymbol{U}_i + \boldsymbol{\xi}_i, \\ \dot{\phi}_i &= \chi_i + \omega_0 + \frac{1}{2}\Omega_z - \sum_{k \neq i} \mu(|\boldsymbol{r}_i - \boldsymbol{r}_k|) \sin(\phi_i - \phi_k), \end{aligned} \tag{20.1}$$

where $\omega_0 > 0$ is an intrinsic rotation frequency that gives rise to the circular clockwise motion of the swimmer at the liquid-gas interface. $\vec{U} = (U_x, U_y)$ is the surface velocity field of the fluid, $\Omega_z = (\nabla \times \boldsymbol{U})_z = \partial_x U_y - \partial_y U_x$ is the z–component of the curl of the surface velocity field. Random rotation of the vector $\boldsymbol{p}_i$ is characterized by a Wiener process $\chi_i(t)$ with $\langle \chi_i(t)\chi_k(t')\rangle = 2D_r\delta(t-t')\delta_{ik}$, where D_r is the rotational diffusivity. The two-dimensional vector $\boldsymbol{\xi}_i = (\xi_x, \xi_y)_i$ with $\langle \boldsymbol{\xi}_i(t)\boldsymbol{\xi}_k(t')\rangle = \mathbf{1}_{2\times 2} 2Mk_BT\delta(t-t')\delta_{ik}$ represents the translational noise, where $\mathbf{1}_{2\times 2}$ is a unit 2×2 matrix, M is the mobility of a single swimmer and T is the absolute temperature.

It is worthwhile to mention the relation of Eq. (20.1) to the previously studied models of self-propelled particles. Thus in case of $\mu = 0$, $\chi = 0$, $\boldsymbol{\xi} = 0$ and $\omega_0 = 0$, the Eq. (20.1) describe a deterministic self-propelled particle that moves in a fluid with a given flow velocity $\boldsymbol{U}$, as considered in Ref. [30]. In the absence of the fluid and without the deterministic rotation, i.e. $\boldsymbol{U} = 0$, $\Omega_z = 0$, $\omega_0 = 0$ and $\boldsymbol{\xi} = 0$ the system Eq. (20.1) reduces to a swarming model, studied in Ref. [9]. For non-interacting and non-rotating swimmers, i.e. for $\mu = 0$ and $\omega_0 = 0$, Eq. (20.1) in conjunction with the thin film equation, have been studied in Ref. [18].

The Smoluchowski equation, derived from Eq. (20.1), for the surface density of swimmers $\rho(\boldsymbol{r}, \phi, t)$ is then given by

$$\partial_t \rho + \nabla \cdot \boldsymbol{J}_t + \partial_\phi J_\phi = 0, \tag{20.2}$$

with translational and rotational currents $\boldsymbol{J}_t$ and J_ϕ, given respectively by

$$\begin{aligned} \boldsymbol{J}_t &= v_0 \boldsymbol{p}\rho + \boldsymbol{U}\rho - Mk_BT\nabla\rho, \\ J_\phi &= \left(\omega_0 + \frac{1}{2}\Omega_z\right)\rho - D_r\partial_\phi\rho - \int\int d\phi' d\boldsymbol{r}' \rho_2(\boldsymbol{r}, \phi, \boldsymbol{r}+\boldsymbol{r}', \phi')\mu(r')\sin(\phi-\phi'), \end{aligned} \tag{20.3}$$

where ρ_2 is the two-particle density function.

Following [9], we employ a mean-field approximation and replace the two-body density $\rho_2(\boldsymbol{r}, \phi, \boldsymbol{r}+\boldsymbol{r}', \phi')$ in Eq. (20.3) by $\rho(\boldsymbol{r}, \phi)\rho(\boldsymbol{r}+\boldsymbol{r}', \phi')$. Next, we recall that the coupling strength $\mu(r')$ rapidly decays with the distance r' between the swimmers. This allows us to expand $\rho(\boldsymbol{r}+\boldsymbol{r}', \phi')$ about $\boldsymbol{r}$ and truncate the expansion after a certain number of leading terms. As shown in Ref. [9], in order to recover a finite wave length instability, one should retain quartic terms $\sim(\boldsymbol{r}')^4$ in the density expansion.

The resulting rotational current can be written as

$$J_\phi = \left(\omega_0 + \frac{1}{2}\Omega_z\right)\rho - D_r\partial_\phi\rho - \rho(\boldsymbol{r}, \phi)\left[\sin\phi\,\hat{\mu}C(\boldsymbol{r}) - \cos\phi\,\hat{\mu}S(\boldsymbol{r})\right], \tag{20.4}$$

where

$$C(\boldsymbol{r}) = \int_0^{2\pi} \rho(\boldsymbol{r}, \phi')\cos\phi' d\phi', \quad S(\boldsymbol{r}) = \int_0^{2\pi} \rho(\boldsymbol{r}, \phi')\sin\phi' d\phi' \tag{20.5}$$

and the operator $\hat{\mu}$ is given by

$$\hat{\mu} = \mu_0 + \mu_2 \Delta + \mu_4 \Delta^2, \tag{20.6}$$

with $\Delta = \nabla^2$. The coefficients μ_0, μ_2 and μ_4 in Eq. (20.6) can be explicitly written as functionals of the coupling strength $\mu(r)$ [9].

Swimmers at the liquid-gas interface may excrete metabolic products that act as a surfactant and change the local surface tension $\sigma(\boldsymbol{r})$ of the liquid film. This phenomenon, called the soluto-Marangoni effect, typically implies a linear decrease of $\sigma(\boldsymbol{r})$ due to the local surface concentration of swimmers $\langle\rho\rangle(\boldsymbol{r}) = \int_0^{2\pi} \rho(\boldsymbol{r}, \phi)\, d\phi$ (cf. Ref. [24]):

$$\sigma(\boldsymbol{r}) = \sigma_0 - \Gamma \langle\rho\rangle(\boldsymbol{r}), \tag{20.7}$$

where $\Gamma > 0$ and Σ_0 is the reference surface tension in the absence of swimmers.

The thin film equation for the local film thickness $h(\boldsymbol{r}, t)$, derived in the lubrication approximation [14], is then coupled to the average concentration $\langle\rho\rangle$ [1, 18]

$$\partial_t h + \nabla \cdot \left(\frac{h^3}{3\eta} \nabla \left[\sigma_0 \Delta h \right] \right) - \Gamma \nabla \cdot \left(\frac{h^2}{2\eta} \nabla \langle\rho\rangle \right) = 0, \tag{20.8}$$

where η is the dynamic viscosity. The surface fluid velocity $\boldsymbol{U}(\boldsymbol{r})$ is found as a function of the local film thickness h [14]

$$\boldsymbol{U} = -\Gamma \frac{h}{\eta} \nabla \langle\rho\rangle + \frac{h^2}{2\eta} \nabla \left(\sigma_0 \Delta h \right). \tag{20.9}$$

Equations (20.2), (20.8) and (20.9) form a closed system of integro-differential equations for the density $\rho(\boldsymbol{r}, \phi, t)$ and the film height $h(\boldsymbol{r}, t)$.

20.3 Linear Stability of the Homogeneous and Isotropic State

In this section we discuss the linear stability of a spatially homogeneous and isotropic stationary solution of Eqs. (20.2), (20.8) and (20.9), given by $\rho(\boldsymbol{r}, \phi) = \rho_0/(2\pi)$ and $h(\boldsymbol{r}) = h_0$, where ρ_0 is the stationary total swimmer density. Using the ansatz $h = h_0 + \delta h$ and $\rho = \rho_0/(2\pi) + \delta\rho$, we expand the perturbation functions δh and $\delta\rho$ according to

$$\delta h(\boldsymbol{r}, t) = h_0 \int \hat{h}(\boldsymbol{k}) e^{\gamma(\boldsymbol{k})t} e^{i\boldsymbol{k}\boldsymbol{r}}\, d\boldsymbol{k}, \tag{20.10}$$

$$\delta\rho(\boldsymbol{r}, \phi, t) = \lim_{N\to\infty} \frac{\rho_0}{2\pi} \sum_{n=-N}^{N} e^{in\phi} \int W_n(\boldsymbol{k}) e^{\gamma(\boldsymbol{k})t} e^{i\boldsymbol{k}\boldsymbol{r}}\, d\boldsymbol{k}, \tag{20.11}$$

with the Fourier amplitudes $\hat{h}(\boldsymbol{k})$ and $W_n(\boldsymbol{k})$, the wave vector of the perturbation $\boldsymbol{k} = (k_x, k_y)$, and the growth rate $\gamma(\boldsymbol{k})$.

Substituting the expansions Eq. (20.10) into Eqs. (20.2) and (20.8) and linearizing about the steady state, we obtain the eigenvalue problem

$$\gamma(\boldsymbol{k})\boldsymbol{H} = \mathcal{J}(\boldsymbol{k})\boldsymbol{H}, \tag{20.12}$$

with the eigenvector $\boldsymbol{H}$

$$\boldsymbol{H}(\boldsymbol{k}) = (\hat{h}, W_0, W_1, W_{-1}, W_2, W_{-2}, \dots), \tag{20.13}$$

and the Jacobi matrix $\mathcal{J}$, which corresponds to a banded matrix of the structure

$$-\mathcal{J}(\boldsymbol{k}) = \left(\begin{array}{cc|cccccc} T_{11} & T_{12} & 0 & 0 & 0 & 0 & 0 & \dots \\ T_{21} & T_{22} & V^- & V^+ & 0 & 0 & 0 & \dots \\ \hline 0 & V^+ & d_1 - \frac{\hat{\mu}(\boldsymbol{k})}{2} & 0 & V^- & 0 & 0 & \dots \\ 0 & V^- & 0 & d_{-1} - \frac{\hat{\mu}(\boldsymbol{k})}{2} & 0 & V^+ & 0 & \dots \\ 0 & 0 & V^+ & 0 & d_2 & 0 & V^- & \dots \\ 0 & 0 & 0 & V^- & 0 & d_{-2} & 0 & \dots \\ 0 & 0 & 0 & 0 & V^+ & 0 & d_3 & \dots \\ \dots & & & & & & & \end{array}\right). \tag{20.14}$$

Here $\hat{\mu}(\boldsymbol{k}) = \mu_0 - \mu_2 k^2 + \mu_4 k^4$, $k^2 = k_x^2 + k_y^2$, $V^+ = v_0\left(\frac{k_y}{2} + \frac{ik_x}{2}\right)$, $V^- = v_0\left(-\frac{k_y}{2} + \frac{ik_x}{2}\right)$ and $d_m = im\omega_0 + m^2 D_r + Mk_BTk^2$ with $m = \pm 1, \pm 2, \pm 3, \dots$ The (2×2) matrix $\boldsymbol{T}$ in the upper left corner of $\mathcal{J}$ is given by

$$\boldsymbol{T}(\boldsymbol{k}) = \begin{pmatrix} \frac{h_0^3}{3\eta}\sigma_0 k^4 & \frac{\Gamma h_0^2}{2\eta}k^2 \\ \frac{h_0^2}{2\eta}\sigma_0 k^4 & \left(\Gamma\frac{h_0}{\eta} + Mk_BT\right)k^2 \end{pmatrix}. \tag{20.15}$$

In practice, we truncate the expansion in the angle ϕ and only take a certain number of the first N Fourier modes into account. Then, the Jacobi matrix $\mathcal{J}$ is an $(2N+2) \times (2N+2)$ matrix and the truncated eigenvector $\mathcal{H} = (\hat{h}, W_0, W_1, W_{-1}, \dots, W_N, W_{-N})$ is $(2N+2)$ dimensional.

Because the perturbations δh and $\delta\rho$ are both real, the eigenvectors of $\boldsymbol{H}$ satisfy the following symmetry conditions

$$\begin{aligned} \hat{h}(\boldsymbol{k})_\gamma^* &= \hat{h}(-\boldsymbol{k})_{\gamma^*} \\ W_n(\boldsymbol{k})_\gamma^* &= W_{-n}(-\boldsymbol{k})_{\gamma^*}, \end{aligned} \tag{20.16}$$

where the asterisk denotes complex conjugation and the subscript γ indicates that the eigenvector $(\hat{h}(\boldsymbol{k})_\gamma, W_0(\boldsymbol{k})_\gamma, W_1(\boldsymbol{k})_\gamma, W_{-1}(\boldsymbol{k})_\gamma, \dots)$ corresponds to the eigenvalue γ.

In what follows, we non-dimensionalise the evolution equations employing the scaling as in Ref. [18]. Thus, we use h_0 as the vertical length scale, $h_0\sqrt{\sigma_0/\Gamma\rho_0}$ as the horizontal length scale, $\eta h_0\sigma_0/(\Gamma^2\rho_0^2)$ as the time scale and the direction-averaged density of swimmers in the homogeneous state ρ_0 as the density scale.

The complete set of the dimensionless system parameters consists of: the self-propulsion velocity $V = v_0\eta\sigma_0^{1/2}/(\Gamma\rho_0)^{3/2}$, the dimensionless rotational diffusivity $D = D_r h_0\eta\sigma_0/(\Gamma\rho_0)^2$, the translational surface diffusivity $d = k_B T M\eta/(h_0\rho_0\Gamma)$, the rotation frequency $\Omega_0 = \omega_0 h_0\eta\sigma_0/(\Gamma\rho_0)^2$ and the alignment/anti-alignment interaction parameters $\tilde{\mu}_i = \mu_i\eta h_0\sigma_0/(\Gamma^2\rho_0)$. For simplicity we drop the tildes in the dimensionless interaction parameters. The dimensionless evolution equations are summarized in Appendix 1.

In what follows, we focus on the effect of the parameter triplet (V, D, Ω_0) on the linear stability of the homogeneous isotropic state. From here on we fix the interaction parameters at $\mu_0 = 1$, $\mu_2 = -1$, $\mu_4 = -10^{-2}$ that can be achieved by the appropriate choice of the coupling function $\mu(r)$. This choice of μ_i corresponds to the finite wave length instability of the homogeneous distribution of non-rotating swimmers, i.e. $\Omega_0 = 0$, in the absence of the liquid film, as studied in Ref. [9].

20.3.1 Singularity of the Instability at $V = 0$

Linear stability analysis reveals remarkable behaviour of the system at vanishingly small swimming velocity $V \approx 0$. By setting $V = 0$ in Eq. (20.14), the eigenvalue with the largest real part can be found analytically

$$\gamma_{\max}(k) = \frac{\hat{\mu}(k)}{2} - d_{\pm 1} = \pm i\Omega_0 - D - dk^2 + \frac{1}{2}\left(\mu_0 - \mu_2 k^2 + \mu_4 k^4\right). \tag{20.17}$$

The fastest growing wave number $k_{\max}$ and the corresponding growth rate $\mathrm{Re}[\gamma(k_{\max})]$ are

$$(k_{\max})^2 = \frac{2d + \mu_2}{2\mu_4}, \quad \mathrm{Re}[\gamma(k_{\max})] = -D + \frac{\mu_0}{2} - \frac{(2d + \mu_2)^2}{8\mu_4}. \tag{20.18}$$

At $V = 0$, the matrix in the lower right corner of Eq. (20.14) is diagonal. The eigenvectors that corresponds to each of the two complex-conjugate eigenvalues Eq. (20.17), have only one non-zero component: either $W_1 \neq 0$, or $W_{-1} \neq 0$. Indeed, the eigenvector $\boldsymbol{H}^+$ that corresponds to $\gamma(k) = \hat{\mu}(k)/2 - d_1$ is given by $\boldsymbol{H}^+ = (0, 0, W_1, 0, 0, \dots)$. Similarly, the eigenvector $\boldsymbol{H}^-$ that corresponds to $\gamma(k) = \hat{\mu}(k)/2 - d_{-1}$ is given by $\boldsymbol{H}^- = (0, 0, 0, W_{-1}, 0, \dots)$. From the physical point of view this means that the colony of swimmers is unstable for a certain interval of k, however this is a purely orientational instability that is reflected in the first Fourier mode, i.e. $W_{\pm 1} \neq 0$. This orientational instability *does not* translate into the instability of h and W_0, as the orientation averaged density $\int_0^{2\pi} \rho(\boldsymbol{r}\phi)\, d\phi$ is insensitive w.r.t. the orientational order of swimmers.

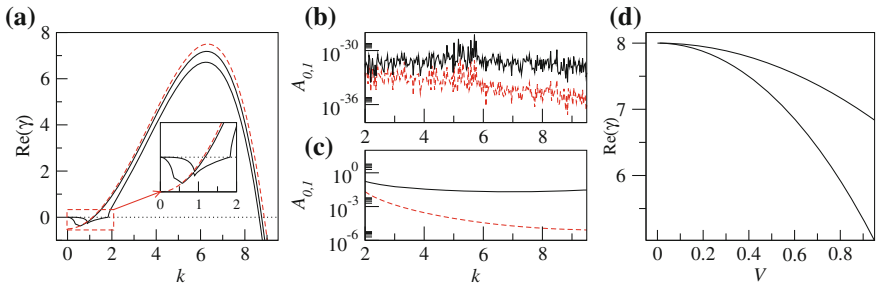

Fig. 20.1 **a** *Solid lines* show the real part of the two largest eigenvalues versus wave number $k = \sqrt{k_x^2 + k_y^2}$ for $V = 0.7$, $D = 1$, $\Omega_0 = 0$ and $d = 0.1$. The *dashed line* corresponds to the dispersion curve at $V = 0$ from Eq. (20.17). The *inset* shows a zoom of the highlighted area near the origin. **b**, **c** Amplitudes $A_0 =\mid \hat{h}(k) \mid^2$ (*dashed line*) and $A_1 =\mid W_0(k) \mid^2$ (*solid line*) of the eigenvectors of the **b** largest and the **c** second largest eigenvalue for $2 < k < 10$ where at least one mode is unstable. **d** Two most unstable eigenvalues $\mathrm{Re}(\gamma)(k_{\max})$ at the fastest growing wave number $k_{\max}$ versus V

Thus, any non-zero velocity $V \neq 0$, no matter how small, introduces the coupling between the first Fourier mode $W_{\pm 1}$ and all other modes W_n, $n = 0, \pm 2, \pm 3, \ldots$, including the amplitude of the film surface deformation $\hat{h}$. As the consequence, the emerging orientational order translates into an instability of the uniform swimmer density and the plane film surface. In order to examine the coupling between the orientational instability of swimmers and the film surface deformations, we set $V = 0.7$, $D = 1$, $\Omega_0 = 0$ and $d = 0.1$ and numerically determine the eigenvalues and the corresponding eigenvectors of the truncated Jacobi matrix Eq. (20.14) with the total number of Fourier modes $N = 50$.

The real parts of the first and the second most unstable eigenvalues are given in Fig. 20.1a as solid lines. The analytic eigenvalue, corresponding to $V = 0$ from Eq. (20.17) is shown by the dashed line. Approximately, for $k > 2$, the first two most unstable eigenvalues for $V = 0.7$ have positive real parts, implying an instability. The fastest growing wave number for $V = 0.7$ is approximately the same as for $V = 0$, i.e. $k_{\max} = \sqrt{40}$ from Eq. (20.18).

By examining the eigenvector that corresponds to the most unstable eigenvalue, we find that the first two components of this eigenvector are given by a numerical zero, i.e. $\mid \hat{h}(k) \mid^2 \sim 10^{-32}$ and $\mid W_0(k) \mid^2 \sim 10^{-32}$, as shown in Fig. 20.1b. This means that the corresponding perturbation is purely orientational and does not couple to the thin film instability. However, the eigenvector of the second most unstable eigenvalue has $\mid \hat{h}(k) \mid^2 \neq 0$ and $\mid W_0(k) \mid^2 \neq 0$, as shown in Fig. 20.1c. This mode corresponds to a simultaneous instability of the film thickness and the average swimmer density.

The singularity of the instability at vanishingly small V is visualized in Fig. 20.1d, where the real parts of the first two most unstable eigenvalues, computed at the fastest growing wave number $k_{\max}$, are plotted against V. We are interested in the second most unstable eigenvalue that corresponds to the coupling between the orientational instability and the film surface deformation. Thus, at any nonzero $V \neq 0$, no matter

how small, the colony of swimmers is linearly unstable with the finite growth rate $\mathrm{Re}[\gamma(k_{\max})] = -D + \mu_0/2 - [(2d + \mu_2)^2]/[8\mu_4]$, as given by Eq. (20.18).

It is important to remark that the role of the thin film in the onset of the instability at vanishingly small V is purely passive. The above described coupling between the orientational instability and the instability of the average density of swimmers $\langle\rho\rangle$ occurs with or without the liquid film, which is linearly stable without the colony of swimmers. However, the situation changes dramatically, if V is finite and if one takes into account the rotation frequency Ω_0, as discussed in the next section.

20.3.2 *Effect of the Liquid Film on the System Stability*

In order to study the effect of the liquid film on the system stability, we distinguish between the film loaded with swimmers and the bare colony of swimmers without the liquid film. Technically, the latter case corresponds to the matrix $\boldsymbol{T}$ in Eq. (20.14), replaced by $T_{11} = T_{12} = T_{21} = 0$ and $T_{22} = Mk_BTk^2$. We numerically solve the eigenvalue problem Eq. (20.14) for the swimmers with and without the liquid film. In the presence of the liquid film, we determine the largest eigenvalue that corresponds to the coupling mode between the orientational instability and the film surface deformation.

We fix $V = 1$, $d = 0.1$ and determine the stability threshold in the plane of parameters (D, Ω_0). In Fig. 20.2a the shaded region marks the values of (D, Ω_0), where

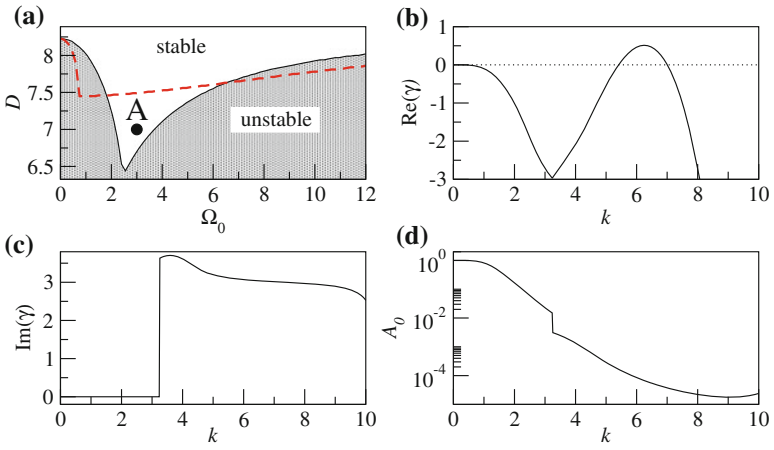

Fig. 20.2 **a** Stability diagram for $V = 1$ and $d = 0.1$. *Shaded area* corresponds to linearly unstable colony of swimmers in the absence of the liquid film. *Dashed line* is the stability threshold for the flat liquid film with swimmers: the system is stable above and unstable below the *dashed line*. In **b**, **c**, **d** we set $D = 7$ and $\Omega_0 = 3$ for a flat liquid film with swimmers (point A in (**a**)): **b** real part, **c** imaginary part and **d** the amplitude $A_0 = |\hat{h}(k)|^2$ of the most unstable eigenvalue versus k

the colony of swimmers is unstable in the absence of the liquid film. For the values of the interaction parameters μ_i chosen here, the homogeneous distribution of swimmers becomes linearly unstable along the border of the shaded region via an oscillatory instability at a finite wave number.

Remarkably, the addition of a stable liquid film, changes the stability threshold dramatically, as shown by the dashed line in Fig. 20.2a. Thus, we find a window of the rotation frequency $2 \lesssim \Omega_0 \lesssim 4$ and of the rotational diffusivity $6.5 \lesssim D \lesssim 7.5$, where the inclusion of a seemingly passive liquid film destabilizes the system. The dispersion curve $\mathrm{Re}(\gamma)(k)$ computed for $D = 7$ and $\Omega_0 = 3$ (point A in Fig. 20.2a) is shown in Fig. 20.2b. In Fig. 20.2c, d we plot the imaginary part of the most unstable eigenvalue and the amplitude $A_0 =\mid \hat{h}(k) \mid^2$ versus k, respectively. The finite values of $\mid \hat{h}(k) \mid^2$ confirm the coupling between the orientational instability and the deformation of the film surface.

Our results show that a colony of swimmers that move on top of a deformable liquid film is less stable than the bare system of swimmers in the case when the film is absent. Such effects are also known for passive systems where e.g. for a film of a binary mixture, the decomposition process couples to the dewetting process in such a way that the flat film becomes linearly unstable. However, the flat film remains linearly stable w.r.t. the each process separately: i.e. it is stable w.r.t. the dewetting and stable w.r.t. the decomposition process [25]. Another example of a coupled system that is less stable than each of its components when decoupled, is a two-layer liquid film on a solid substrate [16, 17]. Thus, for certain immiscible polymer films of different film thickness, placed on top of each other, a two-layer film can be linearly unstable due to weak van der Waals forces that exists between apolar molecules. However, when separated, each of the two layers supported by the same substrate may be linearly stable.

20.4 Nonlinear Evolution from a Homogeneous Isotropic State

The nondimensional evolution equations for the swimmer density $\rho(\boldsymbol{r}, \phi, t)$ and the local film thickness $h(\boldsymbol{r}, t)$ are summarized in Appendix 1. In order to numerically solve the system of Eq. (20.22), we discretize the film thickness $h(x, y, t)$ in a square box $-L \times L$ and the density $\rho(x, y, \phi, t)$ in a rectangle $(x \in [-L/2, L/2]) \times (y \in [-L/2, L/2]) \times (\phi \in [0, 2\pi])$ with periodic boundaries. We use 100×100 mesh points for the discretisation in space and 20 Fourier modes for the decomposition of the ϕ-dependency. We adopt a semi-implicit pseudo-spectral method for the time integration, as outlined in Appendix 2. In order to quantify the patterns, we introduce three global measures: the space-averaged mode type M

$$M = L^{-2} \int \int (h(x, y, t) - 1)(\langle \rho \rangle(x, y, t) - 1)\, dxdy, \tag{20.19}$$

the space-averaged flux of the fluid $\bar{\boldsymbol{J}}_h$, determined by

$$\bar{\boldsymbol{J}}_h = L^{-2} \int \int \left[(h^3/3) \nabla (\Delta h) - (1/2) \left(h^2 \nabla \langle \rho \rangle \right) \right] dxdy \tag{20.20}$$

and the space-averaged orientation field from Eq. (20.5)

$$(\langle C \rangle(t), \langle S \rangle(t)) = L^{-2} \int \int dxdy \, (C(x, y, t), S(x, y, t)) \tag{20.21}$$

The mode type M can be used to analyse the phase shift between the patterns of h and $\langle \rho \rangle$. Non-zero values of the space-averaged fluid flux $\bar{\boldsymbol{J}}_h$ indicates global propagation of patterns. The active part of the space-averaged translational flux of swimmers in Eq. (20.3) is given by $v_0(\langle C \rangle(t), \langle S \rangle(t))$.

20.4.1 Square Array of Vortices

We demonstrate the destabilizing action of the liquid film by choosing the parameters as in point A in Fig. 20.2a.

The time evolution of the mode type M and of the film height h at arbitrarily chosen point on the film surface (x^*, y^*) are shown in Fig. 20.3a, b, respectively. The amplitudes of the average density $\langle \rho \rangle_{\min}$ and $\langle \rho \rangle_{\max}$ are shown in Fig. 20.3c. After passing a certain relaxation time of approximately $\approx$100 time units, the system reaches a stable time-periodic solution that can be characterized as a standing square wave with a well defined spatial period. A typical snapshot of the average density $\langle \rho \rangle(x, y)$ and of the film thickness $h(x, y)$ taken at $t = 150$ is shown in the lower panels in Fig. 20.3. The spatial period l of the square pattern is $l \approx 2\pi / k_{\max}$, where $k_{\max} = 6.2$ is the fastest growing wave number, as extracted from the dispersion curve in Fig. 20.2b. During the entire time evolution, the space-averaged flux of the fluid $\bar{\boldsymbol{J}}_h$ (not shown here) from Eq. (20.20) is of order of 10^{-6}, dropping to a numerical zero for $t > 100$. As the standing square wave regime is established, the space-averaged orientation Eq. (20.21) is numerically zero (not shown). The temporal oscillation period of the standing wave, $T = 2.1$, is extracted from the evolution of $h(x^*, y^*)$ is shown in the inset of Fig. 20.3b. Interestingly, the mode type M oscillates with only a half of the period, $T/2 = 1.05$, indicating that the pattern oscillates between two identical states that are shifted in space.

In order to gain a better understanding of the different phases of the temporal oscillations of the vortex state, we show in Fig. 20.4 three snapshots of the average density $\langle \rho \rangle(x, y)$ and the film thickness $h(x, y)$ from the zoomed area around the bottom left corner of the domain. In addition, we overlay the density snapshot with the vector field of the average orientation of swimmers $\alpha(C(x, y), S(x, y))$, with a conveniently chosen scaling factor α. The three snapshots are taken over one half of the temporal period, between $t = 150.4$ and $t = 151.2$.

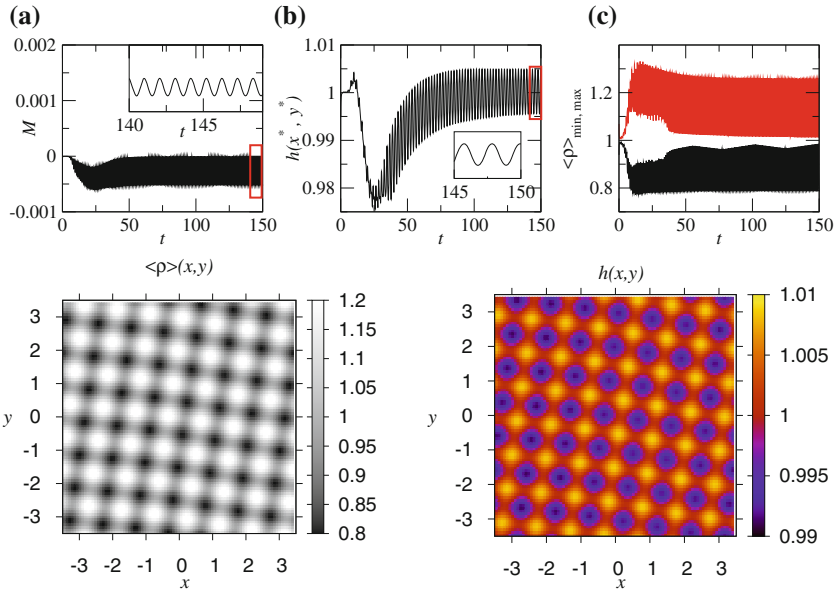

Fig. 20.3 Nonlinear evolution from a homogeneous isotropic state for parameters as in point A in Fig. 20.2a. **a** The mode type M from Eq. (20.19), **b** time evolution of the film height h at an arbitrarily chosen point on the film surface (x^*, y^*) and **c** $\langle\rho\rangle_{\min}$ and $\langle\rho\rangle_{\max}$ as a function of time. *Lower panel* snapshot of the average density $\langle\rho\rangle(x, y)$ and of the film thickness $h(x, y)$ at $t = 150$

At $t = 150.4$ the orientation field is represented by vortices arranged in a square lattice. Vortices located over the depression (elevation) regions of the film thickness profile have an anticlockwise (clockwise) polarity. The average density is in anti-phase with the film profile, implying that the mode type is negative. The dynamics of the vortex polarity can be appreciated from the snapshot taken at $t = 151.0$, where the orientation field is almost radially symmetric. Note that at $t = 151.0$ the depression regions in the average density and in the film thickness profile have turned into the elevation regions and vise-versa. At $t = 151.2$, the polarity of the vortices has reversed as compared with the snapshot taken at $t = 150.4$.

20.4.2 Stripe-Like Density Patterns

Next, we explore the temporal evolution of the system deep in the unstable region. By setting $\Omega_0 = 0$ and $D = 1$ we vary the self-propulsion velocity V and compare the evolution of the swimmers in the absence of the liquid film with the dynamics of the coupled system. Numerically, the Smoluchowski equation is decoupled from the thin film equation by setting $\boldsymbol{U} = 0$ and $\Omega_z = 0$. In the absence of the liquid film we find stripe-like density patterns at small velocities. In Fig. 20.5a the evolution of $\langle\rho\rangle_{\min}$ and $\langle\rho\rangle_{\max}$ is shown by the solid (the dashed) line in the presence (in the

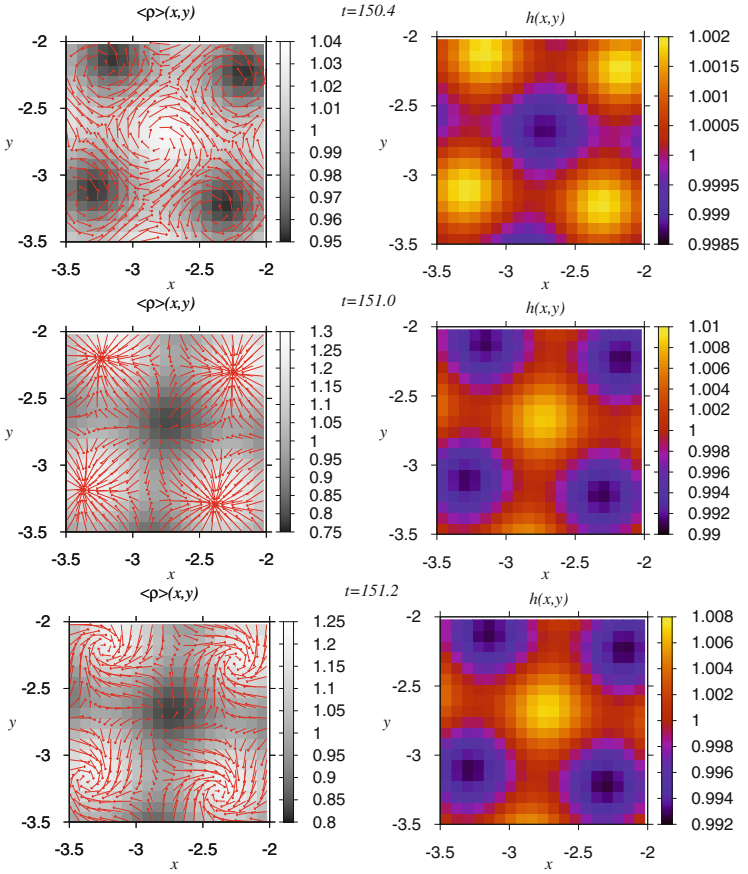

Fig. 20.4 Three snapshots of the average density $\langle\rho\rangle(x, y)$ in grey scale and of the film thickness $h(x, y)$, taken over one half of the oscillation period of the vortex state. The density is overlayed by the vector field of the average orientation of swimmers $\sim(C(x, y), S(x, y))$

absence) of the liquid film. Figure 20.5e shows a snapshot of the density patterns at $t = 100$ in the absence of the film.

The inclusion of the liquid film leads to a significantly smaller amplitude of the average density fluctuations $\langle\rho\rangle_{\max} - \langle\rho\rangle_{\min}$, as can be seen from Fig. 20.5a. In the long time limit, almost parallel stripe-like density patterns are found in the presence of the film as given in Fig. 20.5f. The surface of the film is covered with similar stripe-like patterns that are oriented parallel to the density stripes (Fig. 20.5g). The amplitude of the film surface deformation is of the order of 0.5 % of the average film thickness $h = 1$ (Fig. 20.5b). Stripes on the film surface are in anti-phase with the density stripes, so that the mode type M is negative (Fig. 20.5c). The fluid flux $\bar{\boldsymbol{J}}_h$ is zero in the long time limit (Fig. 20.5d). The space-averaged orientation Eq. (20.21) in the long time limit is a certain non-zero constant (not shown).

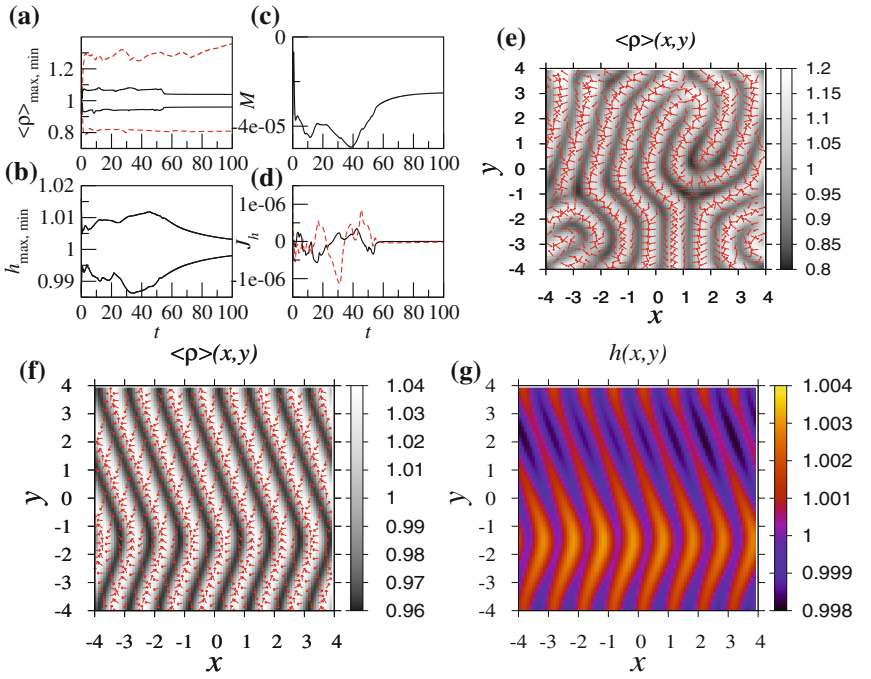

Fig. 20.5 Evolution with and without liquid film at $V = 0.1$, $D = 1$, $\Omega_0 = 0$ and $d = 0.1$. **a**, **b**, **c**, **d** Time evolution of local and global measures. *Solid* (*dashed*) *lines* in (**a**) show $\langle\rho\rangle_{\min}$ and $\langle\rho\rangle_{\max}$ in the presence (in the absence) of the liquid film. *Dashed* and *solid lines* in (**d**) correspond to $(J_h)_x$ and $(J_h)_y$, respectively. **e** Snapshot of the density patterns at $t = 100$ in the absence of the film. **f**, **g** Snapshots of the density patterns and the film surface patterns at $t = 100$ in the presence of the film

20.4.3 Large-Scale Holes in the Film and Film Rupture

When the self-propulsion velocity is increased to $V = 1$, the stripe-like density patterns in the absence of the film are no longer found in the long time limit, as shown in Fig. 20.6f, where we plot the average density field $\langle\rho\rangle(x, y)$ taken at $t = 60$. Instead, the density field corresponds to an irregular time-varying array of high- and low-density spots that have the size of the fastest growing wave length.

In the case, when the film is present, the density field shows maze-like patterns with a typical size comparable to the fastest growing wave length, as given in Fig. 20.6g. These maze-like patterns are overlayed with large-scale modulations with the typical length approximately equal to the domain size. Thus, an elevation region, resembling a droplet, can be seen in the density field in Fig. 20.6g concentrated around $x = -3$, $y = -1$. The film height h is nearly zero in this point, as seen in Fig. 20.6h. The amplitude of density modulations $\langle\rho\rangle_{\max} - \langle\rho\rangle_{\min}$ remains largely unaffected by the liquid film (Fig. 20.6a), fluctuating around the value of $\langle\rho\rangle_{\max} - \langle\rho\rangle_{\min} \approx 1.5$.

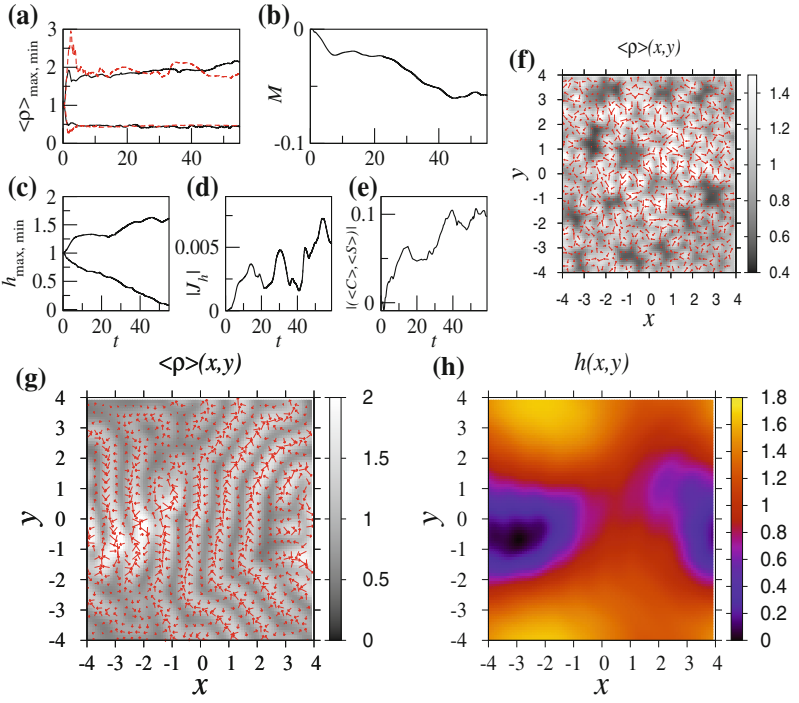

Fig. 20.6 Evolution with and without liquid film at $V = 1$, $D = 1$, $\Omega_0 = 0$ and $d = 0.1$. Line styles in (**a**) as in Fig. 20.5a. Solution measures: **b** the mode type, **c** $h_{\min}$, $h_{\max}$, **d** $\mid \bar{\boldsymbol{J}}_h \mid$ and **e** $|(\langle C\rangle, \langle S\rangle)|$. **f** Snapshot of the density patterns at $t = 60$ in the absence of the film. **g**, **h** Snapshots of the density patterns and the film surface patterns at $t = 60$ in the presence of the film

Remarkably, we find a large-scale hole in the film that develops at a late stage of the time evolution, as shown in Fig. 20.6h. The lateral hole size is of the order of the domain length. The amplitude of the film surface deformations increases with time and, eventually, reaches the point, where $h_{\min} \approx 0$ and the film rupture occurs ($t = 60$ in Fig. 20.6c). The hole in the film is in anti-phase with the elevation region in the average density field, implying negative mode type M in Fig. 20.6b. The magnitudes of the fluid flux $\mid \bar{\boldsymbol{J}}_h \mid$ and the space-averaged orientation $\mid (\langle C\rangle, \langle S\rangle) \mid$ fluctuate randomly with time, as shown in Fig. 20.6d, e, respectively.

From our numerical results we can not definitely decide whether the observed film rupture corresponds to a true finite time singularity or whether it is due to the limited numerical resolution. There exist extensive studies on the rupture of films of simple liquids [4]. In the case of the long-wave thermocapillary instability [3, 13], the film rupture does not seem to occur after finite time. In the case of the destabilising van der Waals interactions [15, 26, 28], the rupture clearly occurs after finite time and close to rupture self-similar solutions can be given. In the model studied here, there are no van der Waals or indeed any other destabilizing (or stabilizing) film surface—substrate

interactions, what makes it unlikely that finite time rupture occurs. However, the issue should be studied in detail in the future, in particular, the role of the interaction of the swimmer density and the film height close to rupture. Average density contains two distinct dominant wave lengths: one is of the order of $2\pi/k_{\max} \approx 1$, and the other one is of the order of the domain size.

20.5 Conclusion

In summary we have considered the dynamics of a colony of swimmers that interact with each other via a short-range alignment and longer-range anti-alignment mechanism and move along the surface of a thin liquid film with deformable liquid-gas interface. We have derived a dynamical model that consists of a thin film equation in the long-wave approximation for the evolution of the local film thickness coupled to the Somluchowski equation for the evolution of the swimmer density function. In contrast to previously used models [1, 9, 18], we have included a deterministic rotation of the swimmers bodies that gives rise to their circular motion along the film surface.

We have focused on the effect of the liquid film on the linear stability of the homogeneous isotropic distribution of swimmers and on its role in the nonlinear time evolution of the system. To this end, we have compared the coupled system of swimmers on the deformable film surface with the bare system of swimmers without a liquid film.

Our results show that the inclusion of the flat film, which is linearly stable without the colony of swimmers on its surface, can induce a finite wave length instability of the isotropic density distribution. This effect is only found for a certain combination of the rotational diffusivity, the self-propulsion velocity and the rotation frequency that gives rise to the circular motion of swimmers. It is not surprising that the coupled system of swimmers on top of a deformable liquid film appears to be less stable than the bare system of swimmers. Generally, a higher degree of complexity of a system implies less stability. Thus, a similar effect was observed earlier for some passive systems that do not contain any active matter [16, 17, 25].

By numerically solving the equations of motion we investigated the nonlinear dynamics of the system from the isotropic state for parameters close to the stability threshold and deep in the unstable region. Close to the stability threshold we found square array of vortices in the density distribution, accompanied by small amplitude deformations of the film surface. Deep in the unstable region, for small values of the self-propulsion velocity, small amplitude stripes in the density field emerge. The film surface remains almost flat with the maximal deformation amplitude reaching as less as 0.5 % of the average film thickness.

For larger values of the self-propulsion velocity, large-scale deep depression forms in the film. The size of the depression is of the order of the domain size and its depth gradually increases with time. The depth of the emerging depression may eventually reach the value of the average film thickness, thus inducing the film rupture.

On a qualitative level, our results can be used to explain the rupture of soaplike liquid films loaded with bacteria, as observed in a series of experiments [20–22]. Without bacteria, any soaplike liquid film, regardless of the film thickness, is linearly unstable due to long-range van der Waals forces that act between apolar molecules that make up the ambient gas layer separated by the liquid film [11]. This implies that even in the ideal case when the evaporation of the liquid can be neglected and the liquid is not drained due to gravity, the flat film is linearly unstable w.r.t. the long-wave deformations of the two liquid-gas interfaces. This instability eventually leads to film rupture after a certain interval of time. The life time of the film is determined by the Hamaker constant that characterizes the strength of the van der Waals interaction, the film thickness h, the surface tension σ and the viscosity of the liquid η. In fact, by using the lubrication approximation [14], it can be shown that the typical life time of the film scales as $\sim h^5 \sigma \eta$.

However, the situation changes dramatically, when the film is loaded with swimmers, whose motion couples to the film deformations via the soluto-Marangoni effect. The orientational instability of the colony of swimmers couples to the instability of the flat film. For films thicker than several μm, the destabilizing action of the van der Waals forces can be neglected as compared with the strength of the orientational instability. In this case, the life time of the film is determined by the typical time scale of the orientational instability, which does not depend on the film thickness. This may explain that surfactant-covered films loaded with bacteria break down earlier than expected.

Appendix 1: Non-dimensional Thin Film Equation and the Smoluchowski Equation

In the here employed dimensionless quantities, the resulting coupled system consists of the reduced Smoluchowski equation for the swimmers density $\rho(\boldsymbol{r}, \phi, t)$ and the thin film equation for the local film thickness $h(\boldsymbol{r}, t)$

$$\partial_t h + \nabla \cdot \boldsymbol{J}_h = 0, \quad \partial_t \rho + \nabla \cdot \boldsymbol{J}_{\mathrm{t}} + \partial_\phi J_\phi = 0, \tag{20.22}$$

with the vorticity of the fluid flow $\Omega_z = \partial_x U_y - \partial_y U_x$, the fluid flux $\boldsymbol{J}_h$, the translational and rotational probability currents $\boldsymbol{J}_t$ and J_ϕ, the surface fluid velocity $\boldsymbol{U}_\parallel$ given by

$$\begin{aligned}
\boldsymbol{J}_h &= (h^3/3)\nabla(\Delta h) - (h^2/2)\nabla\langle\rho\rangle, \quad \boldsymbol{J}_{\mathrm{t}} = (V\boldsymbol{q} + \boldsymbol{U} - d\nabla)\,\rho, \\
J_\phi &= (\Omega_0 + \Omega_z/2)\,\rho - D\partial_\phi\rho - \rho\left[\sin\phi\,\hat{\mu}C(\boldsymbol{r}, t) - \cos\phi\,\hat{\mu}S(\boldsymbol{r}, t)\right], \\
C(\boldsymbol{r}, t) &= \int_0^{2\pi} \rho(\boldsymbol{r}, \phi, t)\,\cos\phi\,d\phi, \quad S(\boldsymbol{r}, t) = \int_0^{2\pi} \rho(\boldsymbol{r}, \phi, t)\,\sin\phi\,d\phi, \\
\hat{\mu} &= \mu_0 + \mu_2\Delta + \mu_4\Delta^2, \quad \boldsymbol{U} = -h\nabla\langle\rho\rangle + h^2/2\nabla(\Delta h)\,.
\end{aligned} \tag{20.23}$$

Appendix 2: Semi-implicit Numerical Scheme for Eqs. (20.22)

The coupled evolution equations Eq. (20.22) are solved numerically using the following version of the semi-implicit spectral method. First, we average the density equation over the orientation angle ϕ. This yields

$$\partial_t \langle \rho \rangle + \nabla \cdot \langle \boldsymbol{J}_{\text{trans}} \rangle = 0, \tag{20.24}$$

with the average translational current $\langle \boldsymbol{J}_{\text{trans}} \rangle = V \langle \boldsymbol{q} \rho \rangle + (\boldsymbol{U} - d\nabla)\langle \rho \rangle$ and $\boldsymbol{q} = (\cos\phi, \sin\phi)$. It is worthwhile noticing that the only term in Eq. (20.24) that depends on the three-dimensional density $\rho(x, y, \phi, t)$ is the average orientation vector $\langle \boldsymbol{q}\rho \rangle$. All other terms in Eq. (20.24), including the surface fluid velocity $\boldsymbol{U}$ explicitly depend on the average density $\langle \rho \rangle$.

Next, we group the thin film equation together with Eq. (20.24)

$$\partial_t h + \nabla \cdot \boldsymbol{J}_h = 0, \quad \partial_t \langle \rho \rangle + \nabla \cdot \langle \boldsymbol{J}_{\text{trans}} \rangle = 0, \tag{20.25}$$

with the fluid flux $\boldsymbol{J}_h = \frac{h^3}{3}\nabla(\Delta h) - \frac{1}{2}\nabla\left(h^2 \nabla \langle \rho \rangle\right)$.

At the next step, we single out the linear parts in all the terms in Eq. (20.25) that explicitly depend on the average density $\langle \rho \rangle$. This is done by linearising the current $\boldsymbol{J}_t$ and the fluid flux $\boldsymbol{J}_h$ about the trivial steady state given by $h = 1$ and $\langle \rho \rangle = 1$.

Next, following the standard implicit time-integration scheme, we replace $\partial_t h$ and $\partial_t \langle \rho \rangle$ by $(h^{t+dt} - h^t)/dt$ and by $(\langle \rho \rangle^{t+dt} - \langle \rho \rangle^t)/dt$, respectively and take all linear terms at time $t + dt$ and all nonlinear terms, including the term $V\langle \boldsymbol{q}\rho \rangle$, at time t. Upon these transformations Eq. (20.25) become

$$\begin{aligned} h^{t+dt} - h^t + (dt/3)\Delta^2 h^{t+dt} - (dt/2)\Delta\langle \rho \rangle^{t+dt} + dt\nabla \cdot (\boldsymbol{N}L_h)^t = 0, \\ \langle \rho \rangle^{t+dt} - \langle \rho \rangle^t + (dt/2)\Delta^2 h^{t+dt} - dt\,(1+d)\,\Delta\langle \rho \rangle^{t+dt} + dt\nabla \cdot (\langle \boldsymbol{N}L_{\text{trans}} \rangle)^t = 0. \end{aligned} \tag{20.26}$$

where NL denotes the nonlinear parts. After taking the discrete Fourier transforms of Eq. (20.26), we find the updated fields h^{t+dt} and $\langle \rho \rangle^{t+dt}$ at the time step $t + dt$.

With the update average density $\langle \rho \rangle^{t+dt}$ and the film thickness h^{t+dt} at hand, we find the updated surface fluid velocity $\boldsymbol{U}^{t+dt}$ and the updated vorticity Ω_z^{t+dt}.

At the next step, we decompose the currents in the second equation in Eq. (20.22) into a linear and a non-linear parts and make use of the semi-implicit integration scheme

$$\rho^{t+dt} - \rho^t + dt\hat{L}\rho^{t+dt} + dt\text{NL}(\rho^t) = 0. \tag{20.27}$$

After taking the Fourier transform of Eq. (20.27) both, in space as well as in the angle ϕ, the operator $\hat{L}_F$ can be written as

$$\hat{L}_F = dk^2 + Dn^2 + in\Omega_0 - 0.5(\delta_{n,1} + \delta_{n,-1})\left(\mu_0 - \mu_0 k^2 + \mu_4 k^4\right). \tag{20.28}$$

The nonlinear part NL is given by

$$\begin{aligned}\mathrm{NL}(\rho^t) = 0.5\Omega_z^{t+dt}\partial_\phi\rho^t + \nabla\cdot(V\boldsymbol{q}\rho^t + \boldsymbol{U}^{t+dt}\rho^t)\\ - \partial_\phi\left(\rho^t - (2\pi)^{-1}\right)\left[\sin\phi(\tilde{\hat{\mu}}C^t) - \cos\phi(\tilde{\hat{\mu}}S^t)\right].\end{aligned} \tag{20.29}$$

By solving Eq. (20.27) w.r.t. ρ^{t+dt} in the Fourier space, we apply the backward Fourier transform and find the updated three-dimensional density $\rho^{t+dt}(x, y)$ in the real space.

References

1. S. Alonso, A.S. Mikhailov, Towards active microfluidics: interface turbulence in thin liquid films with floating molecular machines. Phys. Rev. E **79**, 061906 (2009)
2. I.S. Aranson, A. Sokolov, J.O. Kessler, R.E. Goldstein, Model for dynamical coherence in thin films of self-propelled microorganisms. Phys. Rev. E **75**, 040901 (2007)
3. W. Boos, A. Thess, Cascade of structures in long-wavelength Marangoni instability. Phys. Fluids **11**, 1484–1494 (1999)
4. R.V. Craster, O.K. Matar, Dynamics and stability of thin liquid films. Rev. Mod. Phys. **81**, 1131–1198 (2009)
5. R. Di Leonardo, D. Dell'Arciprete, L. Angelani, V. Iebba, Swimming with an image. Phys. Rev. Lett. **106**, 038101 (2011)
6. Ch. Dombrowski, L. Cisneros, S. Chatkaew, R.E. Goldstein, J.O. Kessler, Self-concentration and large-scale coherence in bacterial dynamics. Phys. Rev. Lett. **93**, 098103 (2004)
7. J. Dunkel, S. Heidenreich, K. Drescher, H.H. Wensink, M. Bär, R.E. Goldstein, Fluid dynamics of bacterial turbulence. Phys. Rev. Lett. **110**, 228102 (2013)
8. P.D. Frymier, R.M. Ford, H.C. Berg, P.T. Cummings, Three-dimensional tracking of motile bacteria near a solid planar surface. Proc. National Acad. Sci. **92**(13), 6195–6199 (1995)
9. R. Großmann, P. Romanczuk, M. Bär, L. Schimansky-Geier, Vortex arrays and mesoscale turbulence of self-propelled particles. Phys. Rev. Lett. **113**, 258104 (2014)
10. T. Ishikawa, N. Yoshida, H. Ueno, M. Wiedeman, Y. Imai, T. Yamaguchi, Energy transport in a concentrated suspension of bacteria. Phys. Rev. Lett. **107**, 028102 (2011)
11. J.N. Israelachvili, *Intermolecular and Surface Forces* (Academic, London, 1992)
12. K.-A. Liu, I. Lin, Multifractal dynamics of turbulent flows in swimming bacterial suspensions. Phys. Rev. E **86**, 011924 (2012)
13. A. Oron, Nonlinear dynamics of three-dimensional long-wave Marangoni instability in thin liquid films. Phys. Fluids **12**, 1633–1645 (2000)
14. A. Oron, S.H. Davis, S.G. Bankoff, Long-scale evolution of thin liquid films. Rev. Mod. Phys. **69**, 931 (1997)
15. D. Peschka, A. Münch, B. Niethammer, Thin-film rupture for large slip. J. Eng. Math. **66**, 33–51 (2010)
16. A. Pototsky, M. Bestehorn, D. Merkt, U. Thiele, Alternative pathways of dewetting for a thin liquid two-layer film. Phys. Rev. E **70**, 025201 (2004)
17. A. Pototsky, M. Bestehorn, D. Merkt, U. Thiele, Morphology changes in the evolution of liquid two-layer films. Phys. Rev. E **122**, 224711 (2005)
18. A. Pototsky, U. Thiele, H. Stark. Stability of liquid films covered by a carpet of self-propelled surfactant particles. Phys. Rev. E (R), **90**, 030401 (2014)
19. I.H. Riedel, K. Kruse, J. Howard, A self-organized vortexarray of hydradynamically entrained sperm cells. Science **309**, 300 (2005)

20. A. Sokolov, I.S. Aranson, Physical properties of collective motion in suspensions of bacteria. Phys. Rev. Lett. **109**, 248109 (2012)
21. A. Sokolov, I.S. Aranson, J.O. Kessler, R.E. Goldstein, Concentration dependence of the collective dynamics of swimming bacteria. Phys. Rev. Lett. **98**, 158102 (2007)
22. A. Sokolov, R.E. Goldstein, F.I. Feldchtein, I.S. Aranson, Enhanced mixing and spatial instability in concentrated bacterial suspensions. Phys. Rev. E **80**, 031903 (2009)
23. Y. Sumino, K.H. Nagai, Y. Shitaka, D. Tanaka, K. Yoshikawa, H. Chate, K. Oiwa, Large-scale vortex lattice emerging from collectively moving microtubules. Nature **483**, 448–452 (2012)
24. U. Thiele, A.J. Archer, M. Plapp, Thermodynamically consistent description of the hydrodynamics of free surfaces covered by insoluble surfactants of high concentration. Phys. Fluids **24**, 102107 (2012)
25. U. Thiele, D.V. Todorova, H. Lopez, Gradient dynamics description for films of mixtures and suspensions: dewetting triggered by coupled film height and concentration fluctuations. Phys. Rev. Lett. **111**, 117801 (2013)
26. D. Tseluiko, J. Baxter, U. Thiele, A homotopy continuation approach for analysing finite-time singularities in thin liquid films. IMA J. Appl. Math. **78**, 762–776 (2013)
27. H.H. Wensink, J. Dunkel, S. Heidenreich, K. Drescher, R.E. Goldstein, H. Lwen, J.M. Yeomans. Meso-scale turbulence in living fluids. Proc. Natl. Acad. Sci. **109**(36), 14308–14313 (2012)
28. T.P. Witelski, A.J. Bernoff, Dynamics of three-dimensional thin film rupture. Phys. D **147**, 155–176 (2000)
29. X.-L. Wu, A. Libchaber, Particle diffusion in a quasi-two-dimensional bacterial bath. Phys. Rev. Lett. **84**, 3017–3020 (2000)
30. A. Zöttl, H. Stark, Nonlinear dynamics of a microswimmer in poiseuille flow. Phys. Rev. Lett. **108**, 218104 (2012)